Applied Catalysis B: Environmental 238 (2018) 51–60

Contents lists available at ScienceDirect

Applied Catalysis B: Environmental

journal homepage: www.elsevier.com/locate/apcatb

Defect-induced efficient dry reforming of methane over two-dimensional Ni/h-boron nitride nanosheet catalysts

Yang Cao[a], Phornphimon Maitarad[a], Min Gao[b,c,**], Tetsuya Taketsugu[b,c], Hongrui Li[a], Tingting Yan[a], Liyi Shi[a], Dengsong Zhang[a,*]

[a] Department of Chemistry, Research Center of Nano Science and Technology, Shanghai University, Shanghai 200444, China
[b] Department of Chemistry, Faculty of Science, Hokkaido University, Sapporo 060-0810, Japan
[c] Elements Strategy Initiative for Catalysts and Batteries, Kyoto University, Kyoto 615-8245, Japan

ARTICLE INFO

Keywords:
Dry reforming of methane
Catalysts
Boron nitride
Density functional calculations

ABSTRACT

Efficient enhancement of catalytic stability and coke-resistance is a crucial aspect for dry reforming of methane. Here, we report Ni nanoparticles embedded on vacancy defects of hexagonal boron nitride nanosheets (Ni/h-BNNS) can optimize catalytic performance by taming two-dimensional (2D) interfacial electronic effects. Experimental results and density functional theory calculations indicate that surface engineering on defects of Ni/h-BNNS catalyst can strongly influence metal-support interaction *via* electron donor/acceptor mechanisms and favor the adsorption and catalytic activation of CH_4 and CO_2. The Ni/h-BNNS catalyst exhibits superior catalytic performance during a 120 h durability test. Furthermore, *in situ* techniques further reveal possible recovery mechanism of the active Ni sites, identifying the enhanced catalytic activities of the Ni/h-BNNS catalyst. This work highlights promotional mechanism of defect-modified interface and should be equally applicable for design of thermochemically stable catalysts.

1. Introduction

Dry reforming of methane (DRM) can utilize CO_2 and CH_4 to produce syngas, which can provide a highly promising solution to the conversion of greenhouse gases into energy-rich mixtures [1,2]. Unfortunately, the DRM reaction requires high temperatures (700–900 °C), most of the catalysts suffered deactivation owing to coking and sintering of metal particles [3,4]. Strong metal-support interactions are well-known to severely affect the catalytic properties of catalysts [5–7]. Therefore, controlling this aspect is highly desirable for both fundamental and practical applications.

Extensive research demonstrated that the two-dimensional (2D) interface can strongly modulate surface chemistry and catalysis, resulting in enhanced or weakened surface reactions [8,9]. 2D hexagonal boron nitride (h-BN), the inorganic analogues of graphene, exhibits many outstanding properties, such as high chemical stability and thermal property, which has been explored for numerous practical applications [10]. It has been demonstrated that h-BN can serve as a unique substrate in harsh processes of heterogeneous catalysis [11]. Grant et al. reported that BN exhibited excellent potential in selectivity to olefins [12]. Particularly, h-BN can provide well-defined 2D layers, which can further enable the occurrence of catalytic reactions in the 2D nanoreactors [13]. While, the pristine h-BN surface is an inert support for metal particles [14], the weak metal-support interaction leads to catalyst deactivation by sintered metal species [15,16]. Well-confined structure can be an effective approach to tune metal-support interaction and promote the metal-catalyzed reactions [13]. For example, core-shell configuration suggests a spatial confinement effects of metal nanoparticles [17,18]. Our previous works demonstrated that the mesoporous SiO_2 can confine and stabilize Ni species towards the DRM reaction. Well-dispersed Ni nanoparticles can provide distinct active sites for the catalytic reaction and inhibit the catalysts deactivation caused by coke formation and metal sintering under the tough conditions [19–21]. Besides the design of well-confined nanostructured catalysts, defect plays a substantial role in modifying the interfacial properties of catalysts by acting as reactive sites and enhancing metal-support interaction [22–24]. Recently, efforts were made to modify the electronic state of catalysts by heteroatom doping in well-defined structural oxides like perovskites [25]. Wang et al. reported the incorporation of Ce into the perovskite can introduce oxygen vacancy defects which provides an effective way to enhance and stabilize DRM activity [26]. For the non-metal oxides, Lei et al. reported that defect-abundant h-BN nanosheets

* Corresponding author at: Department of Chemistry, Research Center of Nano Science and Technology, Shanghai University, Shanghai 200444, China.
** Corresponding author at: Department of Chemistry, Faculty of Science, Hokkaido University, Sapporo 060-0810, Japan.
E-mail addresses: gaomin@sci.hokudai.ac.jp (M. Gao), dszhang@shu.edu.cn (D. Zhang).

https://doi.org/10.1016/j.apcatb.2018.07.001
Received 24 February 2018; Received in revised form 10 May 2018; Accepted 1 July 2018
Available online 02 July 2018
0926-3373/ © 2018 Elsevier B.V. All rights reserved.

(h-BNNS) can be prepared by exfoliation and functionalization methods based on a mechanochemical process [27]. The underlying role of vacancy defects in modulating interface electronic effect and catalytic performance is rarely considered in developing Ni-based catalysts for DRM reaction.

In this work, we suppose to embed Ni nanoparticles in the vacancy-abundant h-BNNS and investigate their structural, surface electronic properties and possible promotional effects in the DRM reaction. According to previous reports [27], a simple mechano-chemical treatment can effectively exfoliate h-BN into nanoscale thickness and water-dispersible h-BNNS (Fig. S1). The h-BNNS supported Ni-based catalyst (denoted as Ni/h-BNNS; Ni loading: 5 wt%; milling time: 20 h) exhibits excellent catalytic activity, stability and coke-resistance. Particularly, there is almost no loss of catalytic activity and carbon deposition even after 120 h durability test. The density functional theory (DFT) calculations illustrate the interfacial electronic effects between Ni and vacancy-abundant h-BNNS (h-BNNS with B vacancy and N vacancy). The defects over the Ni/h-BNNS catalyst interface can strongly enhance the metal-support interaction, which can influence the adsorption and activation of CO_2 and CH_4. Furthermore, *in situ* diffuse reflectance infrared transform spectroscopy (DRIFTs) were performed to reveal the nature of active centers and identify the enhanced catalytic activity of the Ni/h-BNNS catalyst. Ultimately, the reaction mechanisms of the defect-induced efficient DRM reaction over the Ni/h-BNNS interface can be unraveled *via* experimental results and DFT calculations.

2. Experimental section

2.1. Catalyst preparation

2.1.1. Preparation of h-BNNS support

Urea and h-BN (Saint-Gobain Ceramic Materials) were mixed at the weight ratio 1:60, then put the mixtures inside the agate jar and used a planetary ball mill at a rotation speed of 500 r.p.m. for 20 h under N_2 atmosphere [27]. Different milling time (10 h and 30 h) were investigated to seek suitable defective h-BNNS for the preparation of Ni-based catalysts. The obtained white samples were dissolved in deionized water for 7 days to remove the extra urea. Finally, the h-BNNS aqueous dispersions were obtained.

2.1.2. Preparation of Ni/h-BNNS-D serial catalysts

A certain amount of Ni precursor ($Ni(NO_3)_2{\cdot}6H_2O$) was added into the obtained h-BNNS (milling time: 20 h) aqueous dispersions under vigorous stirring at 90 °C. Keep stirring the solution until a thick. The as-prepared mixtures were dried by vacuum freeze drying to maintain the architecture. Finally, the samples were calcined under the air atmosphere at 550 °C for 4 h and reduced under the H_2 at 750 °C for 1 h. The obtained catalyst was denoted as Ni/h-BNNS and the loading of Ni was at 5 wt %. For comparison, the Ni/h-BNNS-D serial catalysts with varying Ni loadings (2% and 10%, milling time: 20 h) were prepared, denoted as Ni/h-BNNS 2% and Ni/h-BNNS 10% catalysts. Furthermore, the Ni/h-BNNS-D serial catalysts with different vacancy-introduced time (milling time: 10 h and 30 h, Ni loading: 5 wt%) of h-BNNS were prepared as well, denoted as Ni/h-BNNS 10 h and Ni/h-BNNS 30 h catalysts.

2.1.3. Preparation of Ni/h-BN catalysts

The Ni/h-BN catalyst were prepared by impregnation process as above mentioned. The support is the pristine h-BN. The Ni loading of the Ni/h-BN catalyst was 5 wt% for comparison.

2.2. Catalyst test

The catalytic activity and stability of the catalysts (120 mg) were conducted in a quartz fixed-bed tubular reactor. The gas mixture of CH_4 and CO_2 ($CO_2/CH_4 = 1$) was introduced at a gas hourly space velocity of 15,000 mL·(gh)$^{-1}$. The gas chromatograph (GC) equipped with TCD analyzed the productions. The catalytic stability was carried out at 750 °C for 20 h and 120 h, respectively. The catalytic activity was sequentially carried out by increasing the reaction temperature from 550 °C to 800 °C. Furthermore, the thermodynamic equilibrium is calculated by HSC software (version 6.0), the calculations included the DRM and reverse water gas reaction (RWGS) reactions.

2.3. In situ study

In situ DRIFTs was performed on a Nicolet 6700 spectrometer with Harrick Scientific DRIFT cell and a mercury-cadumium-telluride detector. The catalysts were purged with N_2 (50 mL·min^{-1}) at 300 °C and got the background spectrum at the room temperature. First, the catalysts pre-adsorbed CO_2 (45 mL·min^{-1}) for 1 h and then introduced CH_4 (45 mL·min^{-1}) stream. The reaction temperature was 500 °C and collected the spectra. Second, the catalysts were pre-adsorbed CH_4 (45 mL·min^{-1}) at 500 °C and then introduced CO_2 (45 mL·min^{-1}) stream to examine the active species. Another experiment is designed to illustrate the process of the DRM reaction, the catalysts were exposed to gas mixtures of CO_2 and CH_4 at 500 °C for 1 h.

2.4. Computational details

The calculations are carried out using density functional theory (DFT) with the functional of Wu and Cohen (WC) as implemented in the SIESTA code [28–30]. Double-ζ plus polarization function (DZP) basis sets are used to treat the $2s^22p^1$, $2s^22p^3$, $2s^22p^4$, $1s^1$ and $4s^23d^8$ valence electrons of B, N, O, H and Ni atoms, respectively [31,32]. The remaining core electrons are represented by the Troullier-Martins norm-conserving pseudopotentials [33] in the Kleinman-Bylander factorized form [34]. The h-BNNS surface is represented by a single layer slab with 7 × 7 element of h-BN. Periodic boundary conditions are used for all systems. All calculations are spin polarized. The energy cutoff of 200 Ry is chosen to guarantee convergence of the total energies and forces. A common energy shift of 10 meV is applied. The atoms in molecules method of Bader (AIM) has been used for charge analysis [35,36]. The energy cutoff of 500 Ry is used to calculated the density of state and Bader charge. The adsorption energy of Ni_2 on h-BNNS is defined as $E_b = E(Ni_2) + E(\text{h-BNNS}) - E(Ni_2/\text{h-BNNS})$ where $E(X)$ denotes the electronic energy of X. The adsorption energy is defined as $E_b = E(Ni_2@\text{h-BNNS}) + E(M) - E(M/Ni_2@\text{h-BNNS})$ where M denotes CH_4 or CO_2. The more positive values of adsorption energy indicate the higher stability of total system.

3. Results and discussion

3.1. Characterization of the catalysts

The morphology and structural properties of the Ni/h-BNNS catalyst are shown in Fig. 1a-f. The Ni particles are homogeneously embedded on the surface of h-BNNS and the particle sizes are mainly ranged from 8 nm to 10 nm. The lattice fringes with a spacing of 0.209 nm can be assigned to the (111) planes of metallic Ni (Fig. 1b), in consistency with XRD results. A typical area was selected to identify the vacancy defects on the exterior surface of the h-BNNS support, and the red arrows suggest the defective regions (Fig. 1c). The vacancies sites can be obviously observed as compared with h-BN materials (Fig. S2). The defect vacancies may influence the interaction between Ni and support, leading to the various dispersion and particle size of the Ni species. In addition, the Ni/h-BNNS-D serial catalysts with varying Ni loadings and milling times also show the homogeneously dispersed Ni species, while, the Ni/h-BN catalyst exhibits the lager Ni particles (Fig. 1d and Fig. S3). The SEM images present the nanoscale thickness and lateral size of the Ni/h-BNNS catalyst after mechano-chemical exfoliation as compared with the Ni/h-BN catalyst (Fig. 1e and Fig. S4), the exfoliated h-BNNS

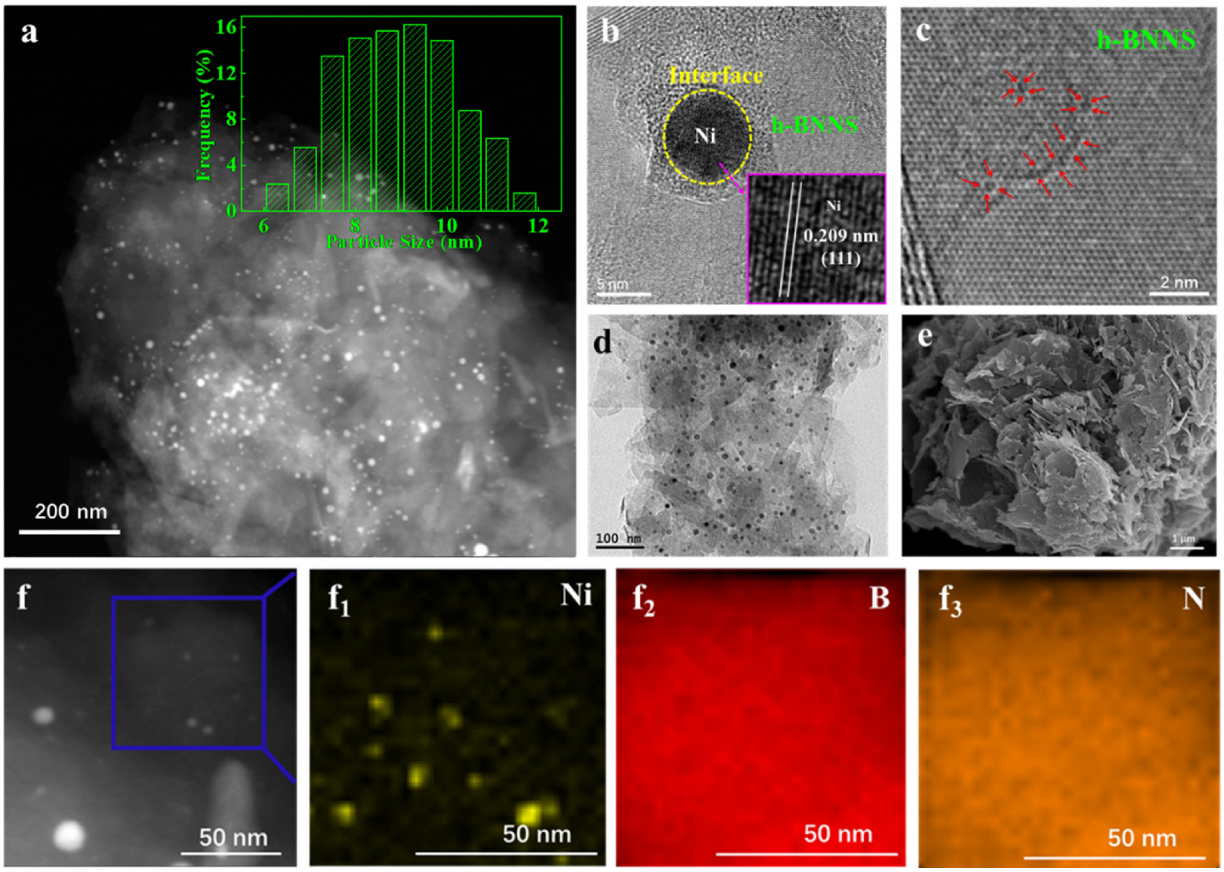

Fig. 1. (a) STEM image with the size distributions of Ni particles and (b) HRTEM image of Ni/h-BNNS catalyst; (c) HRTEM image of h-BNNS materials; (d) TEM image, (e) SEM image and (f) elemental mapping results for the Ni/h-BNNS catalyst.

may expose more edges and corners, proving adequate active sites. Furthermore, the individual phase compositions were confirmed by the STEM-EDX analyses, further illustrating the nano-sized and highly dispersed Ni particles over the 2D interface (Fig. 1f). In addition, CO pulse chemisorption was carried out to identify the Ni dispersion (Table S1). Both the Ni dispersion values of Ni/h-BN and Ni/h-BNNS catalysts are extremely low. Deep and detailed investigation is needed to detect the metal dispersion when considering that both Ni and support have strong interaction with H_2 and CO molecules [37,38].

N_2 adsorption-desorption isotherms characterized the textural property of the Ni/h-BNNS catalyst. The BET specific surface area is 81 m^2/g and the average pore diameter is 3.8 nm (Fig. 2a). The characteristic XRD diffraction peaks corresponding to Ni (111), (200), and (220) are detected (Fig. 2b) over the Ni/h-BNNS and Ni/h-BN catalysts. Notably, the XRD peaks of h-BN phases over the Ni/h-BNNS catalyst decrease significantly, indicating the presence of h-BNNS after mechano-chemical exfoliation [39]. Furthermore, the h-BN phases of the Ni/h-BNNS catalyst shift to the lower angle, which may be due to that the embedded Ni atoms can increase lattice spacing. The expanded region (Fig. 2b and Fig. S5a) can well illustrate that h-BNNS phases shift progressively to the lower angle with the increase of milling time, indicating the degree of incorporation of Ni species into the vacancy defects. The different degree of nano-socketed Ni species may correspond to various exposed active Ni sites, which would influence the catalytic performance. In addition, the weakened characteristic peaks of the h-BN phases with different milling time (10 h, 20 h, 30 h) were also detected in the XRD patterns (Fig. S5).

The microstructure caused by vacancy defects has a great influence on the optical properties [40]. The UV–vis absorption spectra (Fig. 2c) show that, compared to that of Ni/h-BN catalyst, the optical absorption of the Ni/h-BNNS catalyst shifts in the long wavelength range as a result of the abundant defects [40,41]. Furthermore, the optical absorption of few-layer h-BNNS exhibits red-shift as well, which may suggest that defects such as vacancies are inevitably introduced (Fig. S6). Thus, the abundant vacancies of the h-BNNS can offer a great potential to embrace Ni species [24].

3.2. Interaction of Ni species with defect-modified support

According to the H_2-TPR profiles, all catalysts exhibit two or three distinct reduction peaks. Typically, the higher reduction temperature can correspond to the enhanced metal-support interaction [42]. The first peak at lower reduction temperature may suggest weak interaction between NiO and support or small amount of bulk NiO species. While, the reduction peak at the higher temperature can present the stronger metal-support interaction. The Ni/h-BNNS catalyst presents the higher reduction temperature as compared with that of the Ni/h-BN catalyst (Fig. 3a). Therefore, the introduction of abundant defects of the Ni/h-BNNS catalyst can promote the metal-support interaction. In addition, Ni/h-BNNS-D serial catalysts with varying Ni loadings and milling times were evaluated (Fig. S7). We have prepared h-BNNS support with various milling time (10 h, 20 h and 30 h). The increase of milling time may introduce different amount of surface defects. The Ni/h-BNNS-D catalysts with different vacancy-introduced time show the higher reduction temperature and appear at 722 °C (Ni/h-BNNS 10 h), 650/712 °C (Ni/h-BNNS 20 h), and 723 °C (Ni/h-BNNS 30 h), respectively. While, among these catalysts with different milling time, the Ni/h-BNNS (20 h) catalyst presents moderate reduction temperature which may result from highly dispersed Ni species and promoted redox property *via* electron donor/acceptor mechanisms. The DFT calculations and XPS spectra will further demonstrate enhanced redox property of the catalyst. Therefore, taming 2D interfacial electronic effects

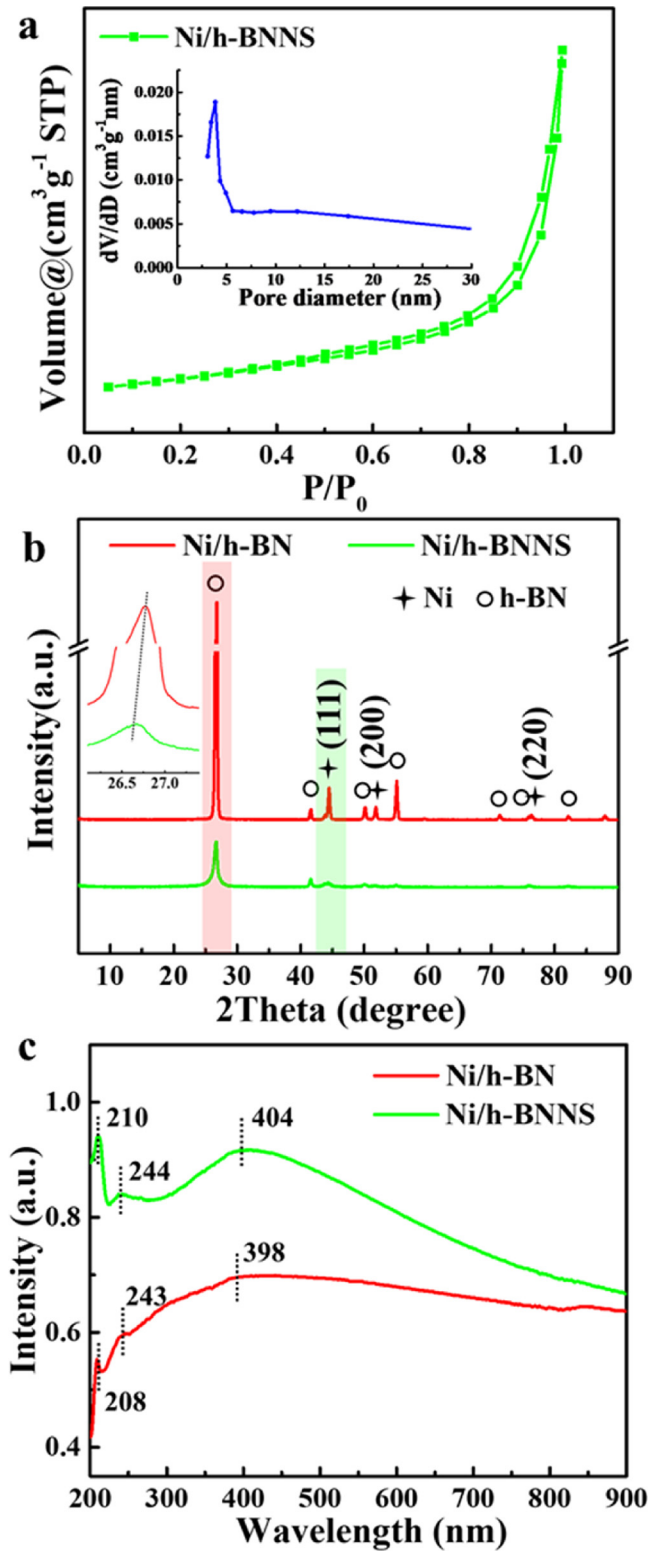

Fig. 2. (a) N_2 adsorption-desorption isotherms of the Ni/h-BNNS catalyst. (b) XRD patterns and (c) UV–vis spectra of the Ni/h-BNNS and Ni/h-BN catalysts.

via control of milling time can well optimize metal-support interaction, which is important to promote the catalytic performance. In addition, the reduction temperatures of Ni/h-BNNS-D catalysts decrease with increasing Ni loadings (612/710 °C for Ni/h-BNNS 2%, 650/712 °C for Ni/h-BNNS 5%, and 416/517/742 °C for Ni/h-BNNS 10%). The differences of reduction temperature can be associated with different Ni dispersion controlled by Ni loadings.

The surface electronic states of the catalysts were explored by X-ray photoelectron spectroscopy (XPS). The XPS whole spectra show the presence of Ni, B, and N in the reduced catalyst (Fig. S8). Notably, the Ni content of the Ni/h-BNNS catalyst is obviously lower than that of the Ni/h-BN catalyst, which further evidences the highly dispersed Ni species through the controllable introduction of vacancy defects. The spectra of Ni 2p exhibit two sets of peaks with binding energies of 853.4 eV and 870.4 eV assigned to Ni°, and 856.4 eV and 874.2 eV attributed to Ni^{2+} (Fig. 3b) [43,44]. The co-existences of the redox cycle (Ni°/Ni^{2+}) can suggest the enhanced redox property of the catalyst [1,45]. In addition, the nano-sized Ni° particles are intrinsically prone to getting oxidized when exposed to air. Notably, the higher Ni 2p binding energies of the Ni/h-BNNS catalyst than the Ni/h-BN catalyst can be consistent with the formation of electron deficient Ni particles *via* electron transfer to the h-BNNS support [46]. DFT calculations with WC functional [47] were carried out to investigate the adsorption of Ni clusters on pristine h-BN and defected h-BNNS, which can further prove the differentiation of the electronic interaction through the control of various defects.

3.3. DFT calculations about electronic properties of the catalysts

According previous theoretical studies, the trends of the charge transfer between metal cluster and surface, and the properties of Ni atoms at the interface will not change by the clusters size. Here, we chose Ni dimer to clarify the interaction between Ni clusters and h-BNNS [48–51]. As shown in Fig. 4, several adsorption structures were located for Ni_2 on pristine h-BN, h-BNNS with B vacancy (V_B_h-BNNS) and h-BNNS with N vacancy (V_N_h-BNNS). Ni_2 adsorbs on the pristine h-BN surface with an adsorption energy of 1.65 eV. With introducing defects, the interaction between Ni_2 and the h-BNNS support becomes considerably stronger. The distance between Ni atoms and h-BNNS with defects are shorter compared to the pristine h-BN case, which is consistent with the experimental result that the existence of defects in h-BNNS surface highly enhanced the interaction between Ni particles and the h-BNNS surfaces. More importantly, the defects strongly affect the charge transfer between h-BNNS and Ni_2. The Bader charge analysis [35] shows that 0.28 ~ 0.32 electrons are transferred from pristine h-BN to the adsorbed Ni_2, while the defects in h-BNNS highly enhances the charge transfer, and moreover, the electron transfer mechanism changes by introducing different type of defects. It shows that the Ni_2 loses 0.35–1.05 electrons that are transferred to V_B_h-BNNS, while the Ni_2 gets 0.11-0.35 electrons from V_N_h-BNNS. Therefore, the V_B_h-BNNS works as an electron acceptor while V_N_h-BNNS works as an electron donor. The electron pushing and donor/acceptor mechanisms over the Ni/h-BNNS can be used to tune the catalytic activity of the supported Ni species.

To gain more insight into the interaction between Ni_2 and h-BNNS, we compared the partial density of states (PDOS) projected on Ni_2, pristine h-BN and h-BNNS with defects (Fig. S9). The pristine h-BN has a very large band gap ~4.50 eV. The introduction of defects highly influences the electronic structures and additional states appearing near the Fermi level. For the free Ni_2 molecule, the state near the Fermi level are mainly the 3*d* states of Ni atoms. After adsorption of Ni_2 on h-BNNS, the wide overlap between 3*d* states of Ni_2 and the states of h-BNNS indicates the strong interaction between them. The states near Fermi level for V_N_h-BNNS and V_B_h-BNNS disappears and *d* states of Ni_2 still exist. Therefore, the active sites on the surfaces for small molecule may mainly localize on the Ni_2.

3.4. Evaluation of the catalytic activity and stability

The introduction of vacancy defects can obviously influence the electronic structure of the Ni/h-BNNS catalyst as discussed above, which offers reaction interface molecular accessibility and promotes the

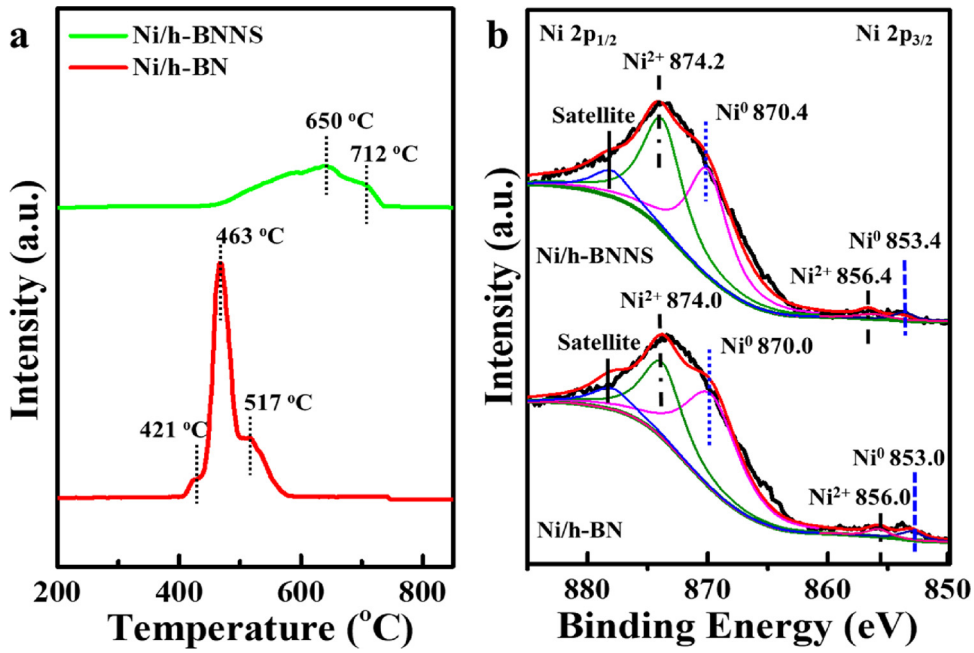

Fig. 3. (a) H_2-TPR profiles and (b) XPS spectra of the reduced catalysts.

catalytic activity. The activities of DRM reaction over the reduced catalysts were evaluated (Fig. 5a). As expected, the Ni/h-BNNS catalyst shows excellent activities at different reaction temperatures (550 °C–800 °C), whereas the lower catalytic activities are observed for the Ni/h-BN catalyst. Notably, CH_4 conversions of the Ni/h-BNNS catalyst is near to thermodynamic equilibrium, especially in the higher temperature range. Simultaneously, there is only 0.2% loss of catalytic activity for the Ni/h-BNNS catalyst even after 120 h stability test (Fig. 5b), illustrating the markedly improved catalytic durability. CO_2 conversion is very important to identify the catalytic performance of the reduced catalysts. As shown in Fig. S10, CO_2 conversions of Ni/h-BN and Ni/h-BNNS catalysts are higher than that of CH_4 conversions, which can be due to the occurrence of reverse water-gas shift reaction (RWGS) [4]. Meanwhile, CO_2 conversion also suggest enhanced catalytic stability of the Ni/h-BNNS catalyst. Furthermore, a serial stability tests of the Ni/h-BNNS-D catalysts were evaluated (Fig. S11) to describe the effects of Ni content and vacancy defects on catalytic stability. For Ni-rich catalysts (Ni loading: 2%, 5%, 10%), the increase of CH_4 conversion can be observed, while for increase of milling time (10 h, 20 h, 30 h), a slight deactivation can be noticed. Based on the result of H_2-TPR and XRD patterns, the Ni/h-BNNS 30 h exists strong metal-support interaction. The partial Ni particles embraced by the h-BNNS allows interaction with amount of exposed Ni sites, which may lead to the decrease of active Ni sites, thus, suggesting rapid deactivation. Therefore, taming the metal-support interaction to optimize metal active-site property is important to control the catalytic performance. Overall, these results and comparisons to the Ni-based catalysts indicate that highly dispersed and nano-sized Ni species can be benefit

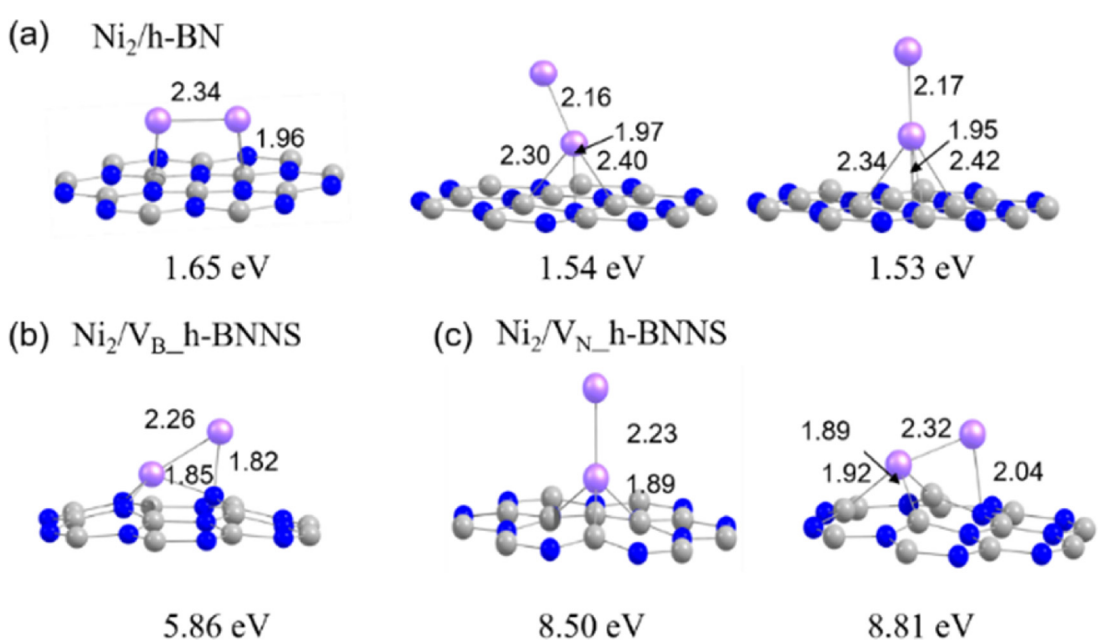

Fig. 4. Adsorption of Ni_2 on (a) pristine h-BN, (b) V_B_h-BNNS and (c) V_N_h-BNNS. The interatomic distances are given in Å. The adsorption energies of Ni_2 on surface are shown below the geometrical structure.

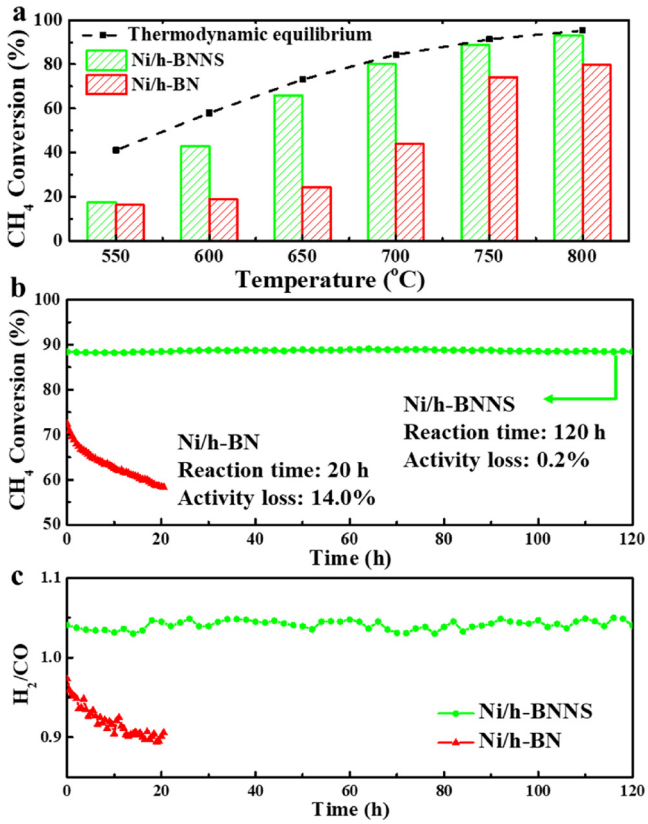

Fig. 5. Temperature dependence of (a) CH_4 conversion, (b) CH_4 conversion as a function of time on stream and relevant (c) H_2/CO ratio over the reduced catalysts.

to the CH_4 conversion [52], while the abundant vacancy defects can further promote the activation of reactant gas, improving their activity and stability.

Moreover, the H_2/CO ratio can quantify the extent of side reactions, demonstrating the catalytic selectivity. We observed that the H_2/CO ratios obtained in the Ni/h-BNNS catalyst are slightly higher than the thermodynamic equilibrium prediction of a H_2/CO ratio of 0.92, whereas Ni/h-BN catalyst shows a lower H_2/CO ratio which decreases significantly from 0.97 to 0.90, illustrating the activity decays (Fig. 5c). The H_2/CO ratio of the Ni/h-BNNS catalyst is slightly higher than 1 is probably due to further side reactions, such as Boudouard reaction or CH_4 decomposition reaction, occur simultaneously [53]. CH_4 decomposition can increase the amount of H_2 and/or Boudouard reaction can decrease the amount of CO, leading to the higher H_2/CO ratio. In addition, these side reactions mainly occur on the Ni sites, and the carbon deposition which may cover the active sites, leading to the catalyst deactivation [54]. For the CH_4 decomposition, it mainly generates highly reactive carbon species C_α which can be gasified by CO_2 [55]. Hence, the elimination of carbon can recover more reactive sites and the anti-coking ability is expected for the Ni/h-BNNS catalyst when compared to the Ni/h-BN catalyst.

3.5. Characterization of the spent catalysts

After the long-term stability test, the Ni/h-BNNS-D catalysts still exhibit highly dispersed Ni species (Fig. S12). Both the experiments and DFT calculations suggested that the vacancy-abundant h-BNNS can enhance the metal-support interaction, resulting in the high dispersion of Ni species and enhanced catalytic performance. On the contrary, for the spent Ni/h-BN catalyst, visually filamentous carbon deposited on the aggregated Ni particles, which can explain the catalyst deactivation. Furthermore, the separation of Ni particles from h-BN support can be observed, attributing to the weak metal-support interaction.

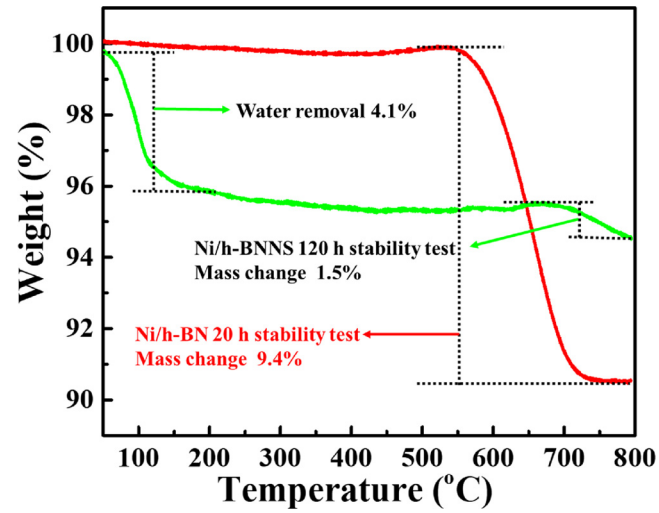

Fig. 6. TG profiles of the spent catalysts after stability test.

In addition, carbon deposition originated from CH_4 decomposition and CO disproportionation on the catalysts during the DRM reaction was quantified by the thermogravimetric analysis (TG). The weight losses of the spent Ni/h-BNNS and Ni/h-BN catalysts after 20 h stability test are 0.3% and 9.4% (Table S2) which are observed in the temperature range 150–800 °C due to the oxidation of carbonaceous species. Remarkably, the Ni/h-BNNS catalyst shows the excellent anti-carbon performance and there is little weight loss even after 120 h stability test (Fig. 6). While, the water loss of the Ni/h-BNNS in the temperature range 50–150 °C can be observed. It may be due to that the surface structure of defective h-BNNS can adsorb an amount of moisture in the air, thus, further illustrating the existence of surface defects. Therefore, we suppose the nano-sized Ni species and abundant defects can synergistically enhance the coke-resistance of the Ni/h-BNNS catalysts. Moreover, the morphology-dependent enhanced the performance of 2D catalysts may be achieved in the DRM reaction. Our previous work focus on the well-defined structure of mesoporous which could enhance sintering and coke resistance of Ni-based catalysts [19–21]. We found that coke formation almost exclusively at the external surface while part of coke formation could occur inside the mesoporous. Internally deposited carbon can cover the Ni species and further block mesoporous, leading to the catalyst deactivation. In addition, it has been reported that external coke causes relatively little hindrance to diffusion [56]. Therefore, we propose that the longer catalytic lifetime of 2D catalysts may be due to the slow coke deposition and gasification of external build-up of coke over the 2D interface.

3.6. In situ study on DRM reactions

To understand the chemistry of DRM process over the Ni/h-BNNS catalyst interface, *in situ* DRIFTs of transient reaction were performed. The Ni/h-BNNS catalyst was pre-adsorbed CH_4 at 500 °C for 1 h. When introducing CO_2 stream, the B—OH vibration peaks linked by H-bonds at 3500-3800 cm^{-1} region appear in Fig. 7a [57,58], as we discussed in the previous study. The intensities of B—OH peaks increase rapidly with flowing CO_2 stream, suggesting that the B—OH species can be formed and adsorbed subsequently on the 2D surface of the Ni/h-BNNS catalyst. Notably, the intensity of the B—OH species maintains after 1 min (Fig. 7b). In comparison, the Ni/h-BNNS catalyst was pre-adsorbed CO_2 at 500 °C for 1 h and then introduced the CH_4 stream simultaneously. While the intensities of the adsorbed B—OH species decrease rapidly with flowing CH_4 stream as a function of time (Fig. 7c), which may illustrate the B—OH species can participate in the DRM reaction. After 1 min, the intensities of B—OH peaks also maintain (Fig. 7d), which is a

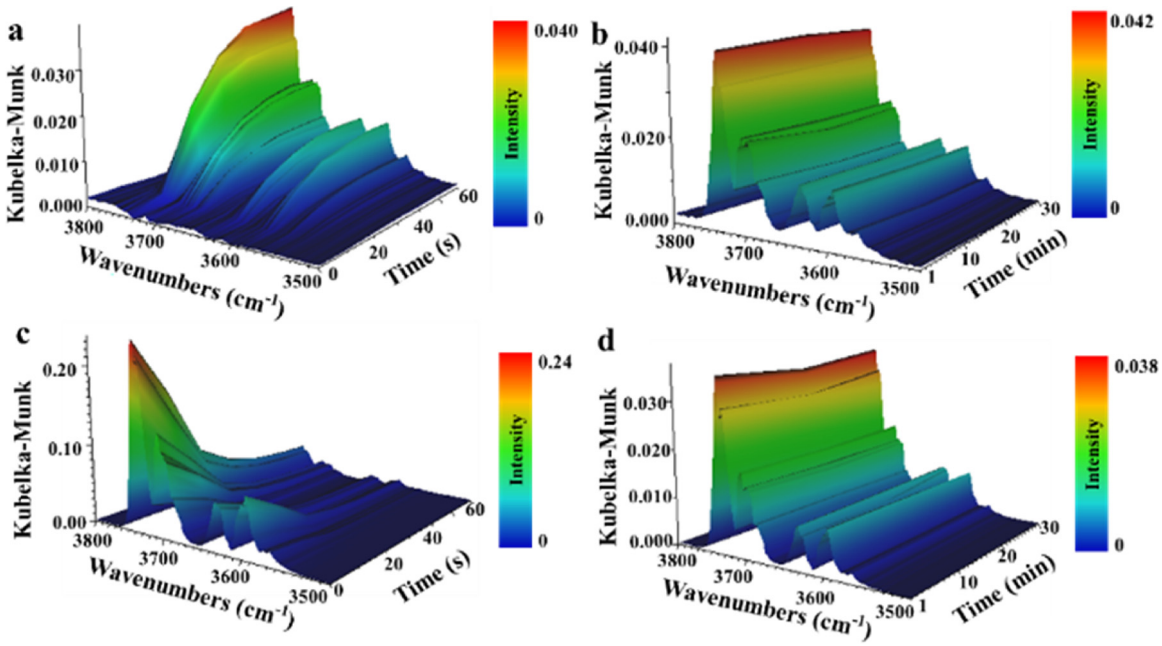

Fig. 7. Evolution of *in situ* DRIFTs over the Ni/h-BNNS catalyst after CH_4 adsorption at 500 °C with flowing CO_2 stream for (a) 1 min and (b) 30 min; and after CO_2 adsorption at 500 °C with flowing CH_4 stream for (c) 1 min and (d) 30 min.

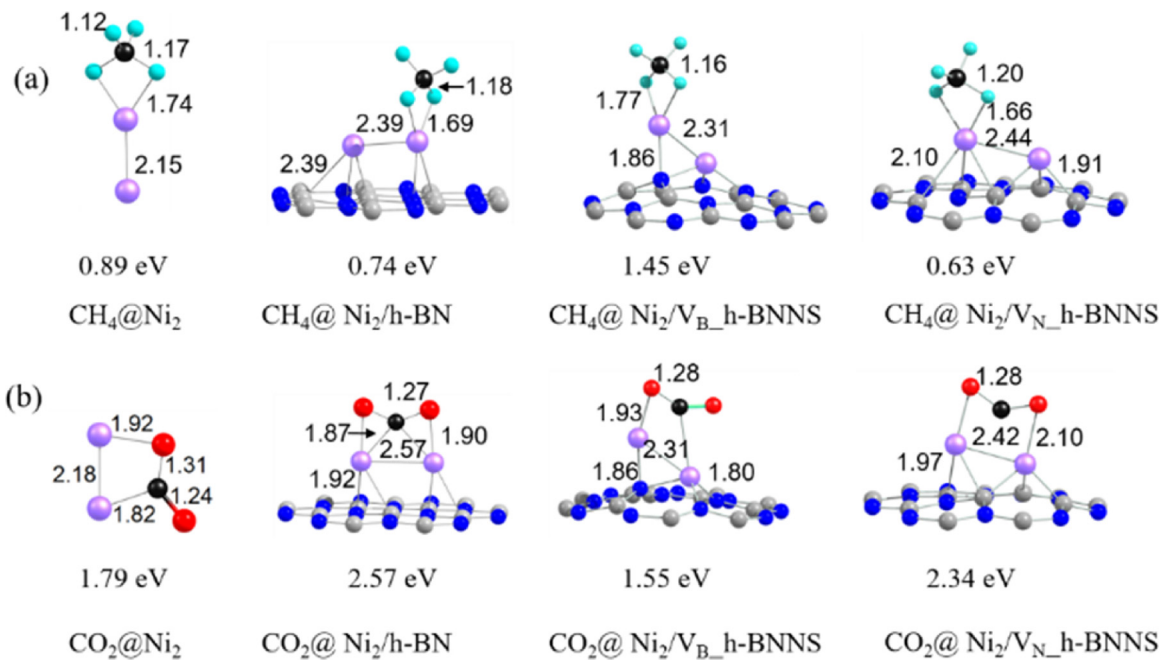

Fig. 8. Adsorption geometry of (a) CH_4 and (b) CO_2 on free Ni_2, Ni_2 supported on pristine h-BN (Ni_2/h-BN), Ni_2 on V_B_h-BNNS (Ni_2/V_B_h-BNNS) and N vacancy (Ni_2/V_N_h-BNNS). The interatomic distances are given in Å. The adsorption energies of Ni_2 on surface are shown below at each structure.

result of the balance between the consumption and generation of B—OH species. Most importantly, we find that the formation of B—OH species can contribute to the improvement of the catalytic activity. During the DRM reaction, it is generally considered that Ni species are the main active sites for the activation of reaction gas, as the DFT calculations discussed. Typically, CH_4 decomposition is mainly occurred over the active Ni sites and formed reactive H and CH_x species which may cover Ni sites [52], thus, easily leading to the catalyst deactivation. While, we find that the intensities of B—OH species decreased when introducing CH_4, which may suggest that the formed H and CH_x species can migrate to the support surface and react with B—OH species. Therefore, we suppose this process can recover more reactive Ni sites and the recovered Ni sites will contribute to the continuous DRM reaction [59]. In addition, *in situ* DRIFTs of the DRM reaction can illustrate the reactivity of the system towards CH_4 and CO_2 over different catalysts. The rate of the formation of B—OH species over the Ni/h-BNNS catalyst is faster than that of Ni/h-BN catalyst (Fig. S13), suggesting the enhanced catalytic activity. It can be ascribed to that abundant vacancy defects can enrich active sites for the DRM reaction.

3.7. Promotional effect of defects on the activation of CH_4 and CO_2

To clarify the effect of h-BNNS surface on the catalytic properties of the Ni nanoparticles, we compared the adsorption and activation of CH_4

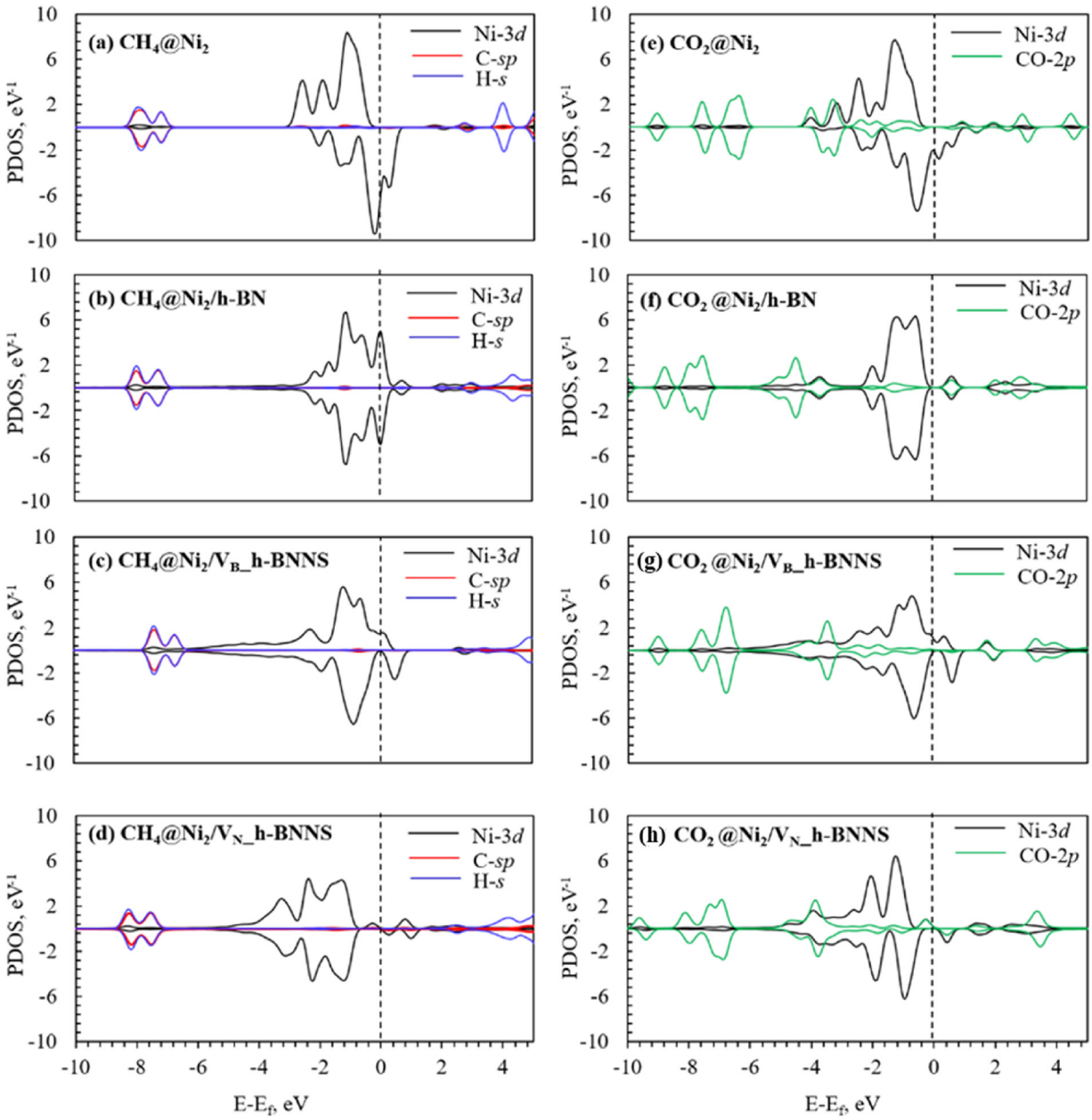

Fig. 9. Partial density of states (PDOS) projected on the Ni_2 (black line), CH_4 and Ni_2 (color line): denote the CH_4 adsorption on (a) free Ni_2, (b) Ni_2/h-BN, (c) Ni_2/V_B_h-BNNS, and (d) Ni_2/V_N_h-BNNS; denote the CO_2 adsorption on (e) free Ni_2, (f) Ni_2/h-BN, (g) Ni_2/V_B_h-BNNS, and (h) Ni_2/V_N_h-BNNS. All the Fermi levels are shifted to 0.0 eV (black line: *3d* orbital of Ni atoms; red line: *sp* orbital of C atom; blue line: *s* orbital of H atom) (For interpretation of the references to colour in this figure legend, the reader is referred to the web version of this article).

and CO_2 on free, pristine h-BN and h-BNNS supported Ni_2. By considering the structures in Fig. 4, the most stable geometries for CH_4 and CO_2 adsorption are shown in Fig. 8. It is demonstrated that the CH_4 prefers to adsorb on the top of Ni_2, while CO_2 prefers to bridge on the Ni-Ni bond. This adsorption geometric properties makes distance between CH_4 and CO_2 on Ni nanoparticles short enough to react with each other. It shows that both CH_4 and CO_2 can adsorb and become activated on the free and h-BNNS supported Ni_2. The existence of V_B can enhance the catalytic activity of the adsorbed Ni_2 for the CH_4 activation. Although the adsorption energy of CH_4 on Ni_2/V_N_h-BNNS is smaller than that in the other cases, the longer bond length of C–H indicates that the CH_4 is highly activated (Fig. 8a). The CO_2 on free and Ni supported surfaces exhibits a bent geometry like anionic CO_2, which indicates the activation of CO_2. The interaction between Ni_2 and h-BN and defected h-BNNS results in significant changes in charge transfer to the adsorbed CO_2. The existence of pristine h-BN and V_N_h-BNNS promotes the charge transfer to the adsorbed CO_2. CO_2 gets less electrons, -0.50 |e| when it adsorbs on the Ni_2/V_B_h-BNNS compared to the free Ni_2 case, -0.66 |e|. Therefore, the more charge transfer from the surface supported Ni_2, the higher activity of Ni_2 for CO_2 adsorption.

Furthermore, we also compared the PDOS projected on Ni_2, pristine h-BN and h-BNNS with defects to investigate the key factors for the activation of CH_4 and CO_2 molecules (Fig. 9). The 3d orbital of Ni atoms, sp orbital of C atom, s orbital of H atom, and sp orbital for CO molecule in CO_2 molecule are extracted to investigate the key factors for the activation of CH_4 and CO_2 molecules over the reduced catalysts. Compared to CH_4@Ni_2, the introduction of h-BNNS does not affect the C-*sp* and H-*s* orbitals are lower than the Fermi level, which means that the σ orbital of C–H is not affected by the additional surfaces. However, the unoccupied orbital around 4.0 eV becomes broader, indicating the

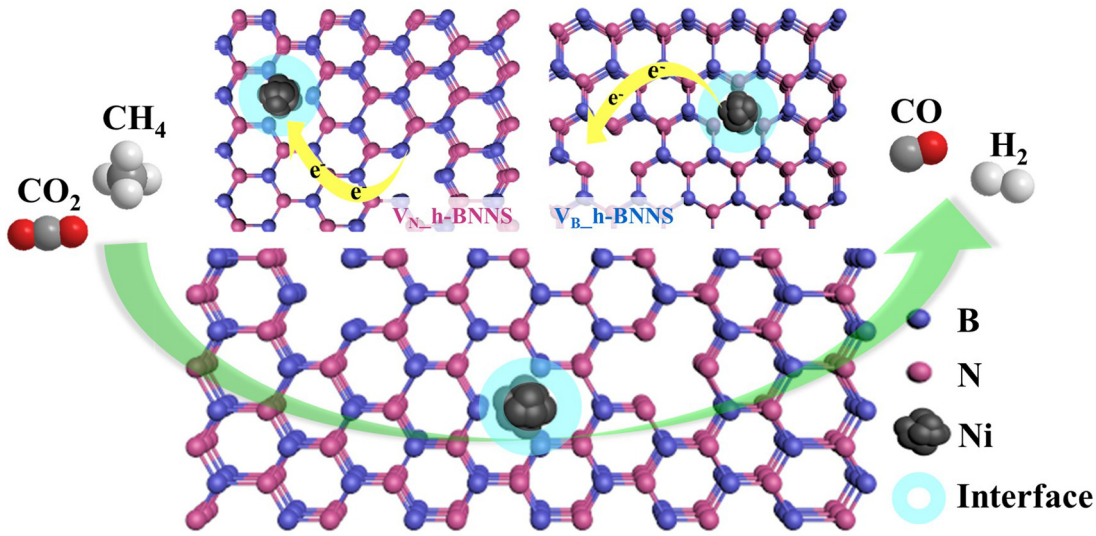

Scheme 1. Proposed reaction mechanism for the DRM reaction over the Ni/h-BNNS catalyst.

stronger interaction between σ* antibonding orbital of CH_4 and surface supported Ni_2. For the case of CO_2 adsorption, the 2*p* of C and O atoms (CO-2*p*) around 3.0 eV changes significantly due to the introduction of h-BNNS, which means the strong interaction between π orbital of CO_2 and 3*d* orbital of Ni atoms. The energy of π states of CO_2 on Ni_2/h-BN and Ni_2/V_N_h-BNNS is lower than the ones on free Ni_2. Therefore, the CO_2 on Ni_2/h-BN and Ni_2/V_N_h-BNNS is more stable and active than on the free Ni_2. The above DFT results are consistent with the experiments and illustrate that various defects of Ni/h-BNNS catalyst can optimize catalytic performance of the DRM reaction by taming 2D interfacial electronic effects.

3.8. Possible reaction mechanism

Overall, the above experimental results, *in situ* studies and DFT calculations demonstrated that the modifying metal-support interaction though vacancy-engineering can be an effective approach to improve the catalytic performance. A proposed mechanism for the DRM reaction on the Ni/h-BNNS catalyst is shown in Scheme 1 and we assess in the following beneficial effects of the interfacial vacancy defects on the catalytic performance: (1) The Ni particles are nano-sized and mainly embedded on vacancy defects of h-BNNS support. The high dispersion and embedded configuration of Ni species can effectively inhibit the metal sintering and enrich active sites for the DRM reaction, leading to superior catalytic durability, indicative of the stronger metal-support interaction. (2) In addition, controlling surface defects of Ni/h-BNNS catalyst can create frustrated Lewis acid-base pairs [60,61]. The V_B_h-BNNS works as an electron acceptor (Lewis acid) while V_N_h-BNNS works as an electron donor (Lewis base). The interfacial electronic properties derived from vacancy defects suggest the enhanced the metal-support interaction, which can favor the activation of CH_4 and CO_2 *via* electron donor/acceptor mechanisms, resulting in the excellent catalytic activity and stability. (3) *In situ* studies identify that the formed B − OH species over the Ni/h-BNNS interface are of great benefit to recover more reactive Ni sites to enhanced catalytic activity. (4) Furthermore, the large number of active sites on the 2D interface render it highly active for the conversion of CH_4 and CO_2 and benefit to the removal of external build-up of carbon, and thereby dramatically inhibits catalyst deactivation caused by the carbon deposition. Overall, the interfacial vacancy doping effectively modified the active sites, morphologies and surface electronic properties, leading to the enhanced the catalytic performance of the Ni/h-BNNS catalyst.

4. Conclusions

In summary, the Ni/h-BNNS catalyst exhibits excellent catalytic activity, stability and coke-resistance during the DRM reaction *via* the synergistic effect of abundant surface defects and nano-sized Ni species. Based on the catalytic performance complemented by *in situ* characterizations and DFT calculations, we reveal key surface electronic properties through the introduction of various defects and identify the catalytic nature of the defect-promoted Ni/h-BNNS catalyst. The richness of vacancy defects over the 2D surface can enhance metal-support interaction *via* electron donor/acceptor mechanisms, which can significantly improve the catalytic conversion of CH_4 and CO_2. Therefore, the vacancy-engineering can be an attractive strategy to optimize catalytic performance by taming interfacial electronic effects. We hope this work can provide new insights into defect effects relevant for the surface applications in energy conversion and storage.

Acknowledgements

The authors acknowledge the support of the National Natural Science Foundation of China (21722704 and U1462110) and the Science and Technology Commission of Shanghai Municipality (17230741400, 16DZ2292100 and 15DZ2281400). This work is partly supported by Grant-in-Aid for Young Scientists (B) (17K1442907) in Japan and partly supported by Ministry of Education, Culture, Sports, Science and Technology (MEXT), Japan, as "Priority Issue on Post-K computer" (Development of new fundamental technologies for high-efficiency energy creation, conversion/storage and use). The computations were partly performed at the Research Center for Computational Science, Okazaki, Japan.

Appendix A. Supplementary data

Supplementary material related to this article can be found, in the online version, at doi:https://doi.org/10.1016/j.apcatb.2018.07.001.

References

[1] S.M. Kim, P.M. Abdala, T. Margossian, D. Hosseini, L. Foppa, A. Armutlulu, W. van Beek, A. Comas-Vives, C. Coperet, C. Muller, Cooperativity and dynamics increase the performance of NiFe dry reforming catalysts, J. Am. Chem. Soc. 139 (2017) 1937–1949.

[2] X. Li, D. Li, H. Tian, L. Zeng, Z.-J. Zhao, J. Gong, Dry reforming of methane over Ni/La_2O_3 nanorod catalysts with stabilized Ni nanoparticles, Appl. Catal. B 202 (2017) 683–694.

[3] X. Zhang, L. Zhang, H. Peng, X. You, C. Peng, X. Xu, W. Liu, X. Fang, Z. Wang, N. Zhang, X. Wang, Nickel nanoparticles embedded in mesopores of AlSBA-15 with a perfect peasecod-like structure: a catalyst with superior sintering resistance and hydrothermal stability for methane dry reforming, Appl. Catal. B 224 (2018) 488–499.
[4] D. Pakhare, J. Spivey, A review of dry (CO_2) reforming of methane over noble metal catalysts, Chem. Soc. Rev. 43 (2014) 7813–7837.
[5] D. Zubenko, S. Singh, B.A. Rosen, Exsolution of Re-alloy catalysts with enhanced stability for methane dry reforming, Appl. Catal. B 209 (2017) 711–719.
[6] J.C. Matsubu, S. Zhang, L. DeRita, N.S. Marinkovic, J.G. Chen, G.W. Graham, X. Pan, P. Christopher, Adsorbate-mediated strong metal-support interactions in oxide-supported Rh catalysts, Nat. Chem. 9 (2017) 120–127.
[7] H. Tang, Y. Su, B. Zhang, A.F. Lee, M.A. Isaacs, K. Wilson, L. Li, Y. Ren, J. Huang, M. Haruta, B. Qiao, X. Liu, C. Jin, D. Su, J. Wang, T. Zhang, Classical strong metal-support interactions between gold nanoparticles and titanium dioxide, Sci. Adv. 3 (2017) e1700231.
[8] Q. Fu, X. Bao, Surface chemistry and catalysis confined under two-dimensional materials, Chem. Soc. Rev. 46 (2017) 1842–1874.
[9] C. Tan, X. Cao, X.J. Wu, Q. He, J. Yang, X. Zhang, J. Chen, W. Zhao, S. Han, G.H. Nam, M. Sindoro, H. Zhang, Recent advances in ultrathin two-dimensional nanomaterials, Chem. Rev. 117 (2017) 6225–6331.
[10] Q. Weng, X. Wang, X. Wang, Y. Bando, D. Golberg, Functionalized hexagonal boron nitride nanomaterials: emerging properties and applications, Chem. Soc. Rev. 45 (2016) 3989–4012.
[11] L. Gao, Q. Fu, M. Wei, Y. Zhu, Q. Liu, E. Crumlin, Z. Liu, X. Bao, Enhanced nickel-catalyzed methanation confined under hexagonal boron nitride shells, ACS Catal. 6 (2016) 6814–6822.
[12] J.T. Grant, C.A. Carrero, F. Goeltl, J. Venegas, P. Mueller, S.P. Burt, S.E. Specht, W.P. McDermott, A. Chieregato, I. Hermans, Selective oxidative dehydrogenation of propane to propene using boron nitride catalysts, Science 354 (2016) 1570–1573.
[13] Y. Zhang, X. Weng, H. Li, H. Li, M. Wei, J. Xiao, Z. Liu, M. Chen, Q. Fu, X. Bao, Hexagonal boron nitride cover on Pt(111): a new route to tune molecule-metal interaction and metal-catalyzed reactions, Nano Lett. 15 (2015) 3616–3623.
[14] J.C.S. Wu, H.-C. Chou, Bimetallic Rh–Ni/BN catalyst for methane reforming with CO_2, Chem. Eng. J. 148 (2009) 539–545.
[15] J. Lu, B. Fu, M.C. Kung, G. Xiao, J.W. Elam, H.H. Kung, P.C. Stair, Coking- and sintering-resistant palladium catalysts achieved through atomic layer deposition, Science 335 (2012) 1205–1208.
[16] J.W. Han, J.S. Park, S.C. Min, H. Lee, Uncoupling the size and support effects of Ni catalysts for dry reforming of methane, Appl. Catal. B 203 (2017) 625–632.
[17] X. Zhang, L. Zhang, H. Peng, X. You, C. Peng, X. Xu, W. Liu, X. Fang, Z. Wang, N. Zhang, X. Wang, Appl. Catal. B 224 (2018) 488–499.
[18] J. Su, C. Xie, C. Chen, Y. Yu, G. Kennedy, G.A. Somorjai, P. Yang, Insights into the mechanism of tandem alkene hydroformylation over a nanostructured catalyst with multiple interfaces, J. Am. Chem. Soc. 138 (2016) 11568–11574.
[19] T. Xie, L. Shi, J. Zhang, Immobilizing Ni nanoparticles to mesoporous silica with size and location control via a polyolassisted route for coking- and sintering-resistant dry reforming of methane, Chem. Commun. 50 (2014) 7250–7253.
[20] X. Du, D. Zhang, R. Gao, L. Huang, L. Shi, J. Zhang, Design of modular catalysts derived from NiMgAl-LDH@m-SiO_2 with dual confinement effects for dry reforming of methane, Chem. Commun. 49 (2013) 6770.
[21] Y. Cao, M. Lu, J. Fang, L. Shi, D. Zhang, Hexagonal boron nitride supported mesoSiO_2 confined Ni catalysts for dry reforming of methane, Chem. Commun. 53 (2017) 7549–7552.
[22] Y. Li, Z. Wei, F. Gao, L. Kovarik, R.A.L. Baylon, C.H.F. Peden, Y. Wang, Effect of oxygen defects on the catalytic performance of VO_x/CeO_2 catalysts for oxidative dehydrogenation of methanol, ACS Catal. 5 (2015) 3006–3012.
[23] G. Li, G.R. Blake, T.T. Palstra, Vacancies in functional materials for clean energy storage and harvesting: the perfect imperfection, Chem. Soc. Rev. 46 (2017) 1693–1706.
[24] W. Zhu, Z. Wu, G.S. Foo, X. Gao, M. Zhou, B. Liu, G.M. Veith, P. Wu, K.L. Browning, H.N. Lee, H. Li, S. Dai, H. Zhu, Taming interfacial electronic properties of platinum nanoparticles on vacancy-abundant boron nitride nanosheets for enhanced catalysis, Nat. Commun. 8 (2017) 15291.
[25] S. Dama, S.R. Ghodke, R. Bobade, H.R. Gurav, S. Chilukuri, Active and durable alkaline earth metal substituted perovskite catalysts for dry reforming of methane, Appl. Catal. B 224 (2018) 146–158.
[26] M. Wang, T. Zhao, X. Dong, M. Li, H. Wang, Effects of Ce substitution at the a-site of $LaNi_{0.5}Fe_{0.5}O_3$ perovskite on the enhanced catalytic activity for dry reforming of methane, Appl. Catal. B 224 (2018) 214–221.
[27] W. Lei, V.N. Mochalin, D. Liu, S. Qin, Y. Gogotsi, Y. Chen, Boron nitride colloidal solutions, ultralight aerogels and freestanding membranes through one-step exfoliation and functionalization, Nat. Commun. 6 (2015) 8849.
[28] Z. Wu, R.E. Cohen, More accurate generalized gradient approximation for solids, Phys. Rev. B 73 (2006) 235116/1-6.
[29] D. Sanchez-Portal, P. Ordejon, E. Artacho, J.M. Soler, Density-functional method for very large systems with LCAO basis sets, Int. J. Quantum Chem. 65 (1997) 453–461.
[30] J.M. Soler, E. Artacho, J.D. Gale, A. Garcia, J. Junquera, P. Ordejon, D. Sanchez-Portal, The siesta method for ab initio order-N materials simulation, J. Phys.: Condens. Matter. 14 (2002) 2745–2779.
[31] E. Artacho, D. Sanchez-Portal, P. Ordejon, A. Garcia, J.M. Soler, Linear-scaling ab-initio calculations for large and complex systems, Phys. Status Solid B 215 (1999) 809–817.
[32] J. Junquera, O. Paz, D. Sanchez-Portal, E. Artacho, Numerical atomic orbitals for linear-scaling calculations, Phys. Rev. B 64 (2001) 235111/1-9.
[33] N. Troullier, J.L. Martins, Efficient pseudopotentials for plane-wave calculations, Phys. Rev. B 43 (1991) 1993–2006.
[34] L. Kleinman, D.M. Bylander, Efficacious form for model pseudopotentials, Phys. Rev. Lett. 48 (1982) 1425–1428.
[35] R. Bader, Atoms in Molecules: A Quantum Theory, Oxford University Press, New York, 1990.
[36] G. Henkelman, A. Arnaldsson, H. Jonsson, A fast and robust algorithm for bader decomposition of charge density, Comput. Mater. Sci. 36 (2006) 354–360.
[37] Q. Weng, X. Wang, C. Zhi, Y. Bando, D. Golberg, Boron nitride porous microbelts for hydrogen storage, ACS Nano 7 (2013) 1558–1565.
[38] W.C. McKee, M.C. Patterson, D. Huang, J.R. Frick, R.L. Kurtz, P.T. Sprunger, L. Liu, Y. Xu, CO adsorption on Au nanoparticles grown on hexagonal boron Nitride/Rh (111), J. Phys. Chem. C 120 (2016) 10909–10918.
[39] W. Zhu, X. Gao, Q. Li, H. Li, Y. Chao, M. Li, S.M. Mahurin, H. Li, H. Zhu, S. Dai, Controlled gas exfoliation of boron nitride into few-layered nanosheets, Angew. Chem. Int. Ed. 55 (2016) 10766–10770.
[40] P. Niu, L.C. Yin, Y.Q. Yang, G. Liu, H.M. Cheng, Increasing the visible light absorption of graphitic carbon nitride (melon) photocatalysts by homogeneous self-modification with nitrogen vacancies, Adv. Mater. 26 (2014) 8046–8052.
[41] Y. Wang, X. Wang, M. Antonietti, Polymeric graphitic carbon nitride as a heterogeneous organocatalyst: from photochemistry to multipurpose catalysis to sustainable chemistry, Angew. Chem. Int. Ed. 51 (2012) 68–89.
[42] S. Das, S. Thakur, A. Bag, M.S. Gupta, P. Mondal, A. Bordoloi, Support interaction of Ni nanocluster based catalysts applied in CO_2 reforming, J. Catal. 330 (2015) 46–60.
[43] L. Pathade, T.L. Doane, R.D. Slaton, M.M. Maye, Understanding the oxidation behavior of Fe/Ni/Cr and Fe/Cr/Ni Core/Alloy nanoparticles, J. Phys. Chem. C 120 (2016) 22035–22044.
[44] H. Ali-Löytty, M.W. Louie, M.R. Singh, L. Li, H.G. Sanchez Casalongue, H. Ogasawara, E.J. Crumlin, Z. Liu, A.T. Bell, A. Nilsson, D. Friebel, Ambient-pressure XPS study of a Ni-Fe electrocatalyst for the oxygen evolution reaction, J. Phys. Chem. C 120 (2016) 2247–2253.
[45] K.A. Choquette, D.V. Sadasivam, R.A. Flowers, Catalytic Ni(II) in reactions of SmI_2: Sm(II)- or Ni(0)-based chemistry? J. Am. Chem. Soc. 133 (2011) 10655–10661.
[46] J. Zhang, C. Zhao, Development of a bimetallic Pd-Ni/HZSM-5 catalyst for the tandem limonene dehydrogenation and fatty acid deoxygenation to alkanes and arenes for use as biojet fuel, ACS Catal. 6 (2016) 4512–4525.
[47] M. Gao, A. Lyalin, T. Taketsugu, Catalytic activity of Au and Au_2 on the h-BN surface: adsorption and activation of O_2, J. Phys. Chem. C 116 (2012) 9054–9062.
[48] H. Xu, W. Chu, W. Sun, C. Jiang, Z. Liu, DFT studies of Ni cluster on graphene surface: effect of CO_2 activation, RSC Adv. 6 (2016) 96545–96553.
[49] A. Cadi-Essadek, A. Roldan, N.H. de Leeuw, Density functional theory study of Ni clusters supported on the ZrO_2 (111) surface, Fuel Cells 17 (2017) 125–131.
[50] A. Cadi-Essadek, A. Roldan, N.H. De Leeuw, Stability and mobility of supported nin (n = 1-10) clusters on ZrO_2(111) and YSZ(111) surfaces: a density functional theory study, Faraday Discuss. (2017), https://doi.org/10.1039/C7FD00217C.
[51] P.G. Lustemberg, P.J. Ramírez, Z. Liu, R.A. Gutiérrez, D.G. Grinter, J. Carrasco, S.D. Senanayake, J.A. Rodriguez, M.V. Ganduglia-Pirovano, Room-temperature activation of methane and dry Re-forming with CO_2 on Ni-CeO_2(111) surfaces: effect of Ce^{3+} sites and metal-support interactions on C-H bond cleavage, ACS Catal. 6 (2016) 8184–8191.
[52] K. Yuan, J.-Q. Zhong, X. Zhou, L. Xu, S.L. Bergman, K. Wu, G.Q. Xu, S.L. Bernasek, H.X. Li, W. Chen, Dynamic oxygen on surface: catalytic intermediate and coking barrier in the modeled CO_2 reforming of CH_4 on Ni (111), ACS Catal. 6 (2016) 4330–4339.
[53] Z. Shang, S. Li, L. Li, G. Liu, X. Liang, Highly active and stable alumina supported nickel nanoparticle catalysts for dry reforming of methane, Appl. Catal. B 201 (2017) 302–309.
[54] S.A. Theofanidis, R. Batchu, V.V. Galvita, H. Poelman, G.B. Marin, Carbon gasification from Fe-Ni catalysts after methane dry reforming, Appl. Catal. B 185 (2016) 42–55.
[55] C.-j. Liu, J. Ye, J. Jiang, Y. Pan, Progresses in the preparation of coke resistant Ni-based catalyst for steam and CO_2 reforming of methane, ChemCatChem 3 (2011) 529–541.
[56] A. Corma, Catalysts made thinner, Nature 461 (2009) 7261.
[57] P. Banerjee, B. Pathak, R. Ahuja, G.P. Das, First principles design of Li functionalized hydrogenated h-BN nanosheet for hydrogen storage, Int. J. Hydrogen Energy 41 (2016) 14437–14446.
[58] G. Zhao, Y. Li, C. Liu, Y. Wang, J. Sun, Y. Gu, Y. Wang, Z. Zeng, Boron nitride substrate-induced reversible hydrogen storage in bilayer solid matrix via interlayer spacing, Int. J. Hydrogen Energy 37 (2012) 9677–9687.
[59] L. Foppa, M.-C. Silaghi, K. Larmier, A. Comas-Vives, Intrinsic reactivity of Ni, Pd and Pt surfaces in dry reforming and competitive reactions: insights from first principles calculations and microkinetic modeling simulations, J. Catal. 343 (2016) 196–207.
[60] J. Sun, R.A. Baylon, C. Liu, D. Mei, K.J. Martin, P. Venkitasubramanian, Y. Wang, Key roles of lewis acid-Base pairs on $Zn_xZr_yO_z$ in direct Ethanol/Acetone to isobutene conversion, J. Am. Chem. Soc. 138 (2016) 507–517.
[61] S. Zhang, Z.Q. Huang, Y. Ma, W. Gao, J. Li, F. Cao, L. Li, C.R. Chang, Y. Qu, Solid frustrated-lewis-pair catalysts constructed by regulations on surface defects of porous nanorods of CeO_2, Nat. Commun. 8 (2017) 15266.